Enhancing nondestructive mass identification via Fourier-transform fluorescence analysis

F. Domínguez,[1] D. Yousaf,[1] J. Berrocal,[1] M. J. Gutiérrez,[1,*] J. Sánchez,[1] M. Block,[2,3,4] and D. Rodríguez[1,5,†]

[1]*Departamento de Física Atómica, Molecular y Nuclear, Universidad de Granada, 18071 Granada, Spain*

[2]*Department Chemie - Standort TRIGA, Johannes Gutenberg-Universität Mainz, 55099 Mainz, Germany*

[3]*GSI Helmholtzzentrum für Schwerionenforschung GmbH, 64291 Darmstadt, Germany*

[4]*Helmholtz-Institut Mainz, 55099 Mainz, Germany*

[5]*Centro de Investigación en Tecnologías de la Información y las Comunicaciones, Universidad de Granada, 18071 Granada, Spain*

(Received 19 July 2024; accepted 9 November 2024; published 10 December 2024)

Single-ion mass identification is important for atomic and nuclear physics experiments on ions produced with low yields. Cooling the ion to ultralow temperatures through interaction with a laser-cooled ion will enhance the precision of the measurements. In this paper we present axial-common-mode frequency measurements of balanced and unbalanced Coulomb crystals from the Fourier transform of the fluorescence photons from a Doppler-cooling transition in calcium ions after probing the ion crystal with a five-radio-frequency comb. A single ion nondestructively detected can be used for identification, yielding a mass-resolving power $m/\Delta m_{\mathrm{FWHM}} \approx 310$ from the axial common mode. This identification can be performed from a single measurement within times below 1 s.

DOI: 10.1103/PhysRevResearch.6.043255

I. INTRODUCTION

Experimental studies of atomic and nuclear observables such as masses, nuclear spins, and electromagnetic nuclear moments are important to understand the peculiar properties of the heaviest elements in the periodic table of chemical elements [1,2]. These nuclides can only be produced artificially in nuclear reactions at accelerator facilities, with very low resulting yields, on the order of ions per second for nuclides with $Z = 102$ down to about one particle per day for $Z = 118$. This calls for single-ion sensitivity for laser spectroscopy or mass spectrometry and also good control and localization of the superheavy element (SHE) ion. For example, the higher spectral resolution needed to resolve the hyperfine splitting [3], required to determine electromagnetic moments and to enable an unambiguous assignment of the nuclear spin, can be attained when cooling the ion to ultralow temperatures by means of Doppler laser cooling. Since this is not yet feasible due to the limited experimental information on atomic transitions and the often complex level structure of the atomic spectra, the SHE ion has to be cooled through another (laser-cooled) ion. The same experimental platform, i.e., an unbalanced Coulomb crystal made of a laser-cooled and a target ion, can provide nondestructive mass identification of the latter [4] and even identification of a molecular ion after some chemical reaction of the SHE ion with reactive gases is induced [5].

The demonstration of mass spectrometry with sympathetically cooled ions was reported in 1996 [6], and it has proved, in the last decade, beneficial to identify stable ions [7] and radioactive ions [8] when working with large ion clouds and when accumulating sufficient statistics, respectively. Single-ion mass spectrometry through Fourier transformation of the fluorescence signal from a laser-cooled stable ion was reported in 2001 [9]. Well-localized atomic and molecular ions in Coulomb crystals were observed around the same time [10,11], followed by the demonstration of nondestructive identification through fluorescence images of balanced and unbalanced two-ion Coulomb crystals [5]. In the latter case, the two ions, with mass-to-charge ratios $m_{\mathrm{s}}/q_{\mathrm{s}}$ and $m_{\mathrm{t}}/q_{\mathrm{t}}$, have sufficiently small kinetic energy to perform small oscillations around their equilibrium positions. In a linear Paul trap with $\omega_z < \omega_{x,y}$, the ions will line up along the z axis. Considering that the ions move with small oscillation amplitudes compared to their separation distance D and defining $\mu = m_{\mathrm{t}}/m_{\mathrm{s}}$ and $\kappa = q_{\mathrm{t}}/q_{\mathrm{s}}$, the axial motion of the system can be described in terms of normal modes, with eigenfrequencies [12]

$$(\Omega_z^{\pm})^2 = \frac{\omega_z^2}{2}\left\{\left[\alpha+\beta\frac{2\kappa}{\kappa+1}\right] \pm \sqrt{\left[\alpha+\beta\frac{2\kappa}{\kappa+1}\right]^2 - 12\frac{\kappa}{\mu}}\right\}, \tag{1}$$

where ω_z is the axial frequency of the single laser-cooled ion $(m_{\mathrm{s}}/q_{\mathrm{s}})$, $\alpha = 1 + \kappa/\mu$, and $\beta = 1 + 1/\mu$. The superscripts $-$ and $+$ represent the common and stretch modes, respectively. When both ions are singly charged ($q_{\mathrm{s}} = q_{\mathrm{t}} = 1$), as is

*Present address: Institut für Physik, University of Greifswald, Germany, GSI Darmstadt, Germany.

†Contact author: danielrodriguez@ugr.es

the case for the experiments presented here, Eq. (1) simplifies to the well-known expressions given in Ref. [13].

Experimentally, if one ion is laser cooled (e.g., the one with mass-to-charge ratio m_s/q_s), the other one will be sympathetically cooled due to the Coulomb interaction [14].

Several identification methods have been developed for ion crystals in Paul traps: (1) resonant excitation of the common mode with a time-oscillating voltage [15], (2) application of periodic voltage pulses to one of the trap electrodes [16], (3) a scan of the motional frequencies $\Omega_z^{\pm}$ through sideband spectroscopy on an electric quadrupole transition with an ultrastable laser [17], (4) determination of the shift in the equilibrium position of the fluorescing ion after the crystal is formed [18], (5) optical amplification of the crystal's motion with lasers [19], and (6) fast switching of the trap center position with a voltage pulse [20]. Methods 1 and 4 are based on the monitoring of the fluorescence signal with an electron-multiplying charge-coupled device (EMCCD) camera, whereas methods 2, 5, and 6 rely on Fourier analysis of the fluorescence signal detected with a photomultiplier tube (PMT). In this work we detect and identify singly charged atomic ions through Fourier analysis of the detected fluorescence photons scattered by the laser-cooled ion in an unbalanced two-ion crystal after probing the crystal with a radio-frequency comb. The foundation relies on the fluorescence modulation due to the crystal's motion in the trap under near-resonant oscillating electric fields and its subsequent Fourier transform to obtain a discrete frequency spectrum around the axial-common mode. The method is fast, nondestructive, and thus suitable for performing experiments in which the highest sensitivity is requested. This is the case of SHEs [21–23], provided the full process before the measurement, which comprises online production, stopping in a gas cell, separation, and subsequent cooling, is carried out with the highest efficiency. We analyze the precision in mass identification obtained with this method in the Doppler regime and discuss the effect of nonlinearities due to the Coulomb interaction.

II. EXPERIMENTAL SETUP

The experimental setup is schematically shown in Fig. 1(a). A sketch of the radio-frequency comb is depicted in Fig. 1(b). The experiments presented here were conducted with two-ion crystals composed of a Doppler-cooled $^{40}Ca^+$ ion and a $^{A}Ca^+$ isotope ($A = 40, 42, 44, 48$). For Doppler cooling and detection of $^{40}Ca^+$, a 10-MHz red-detuned 397-nm diode laser driving the $S_{1/2} \leftrightarrow P_{1/2}$ transition was used. A tunable 866-nm diode laser was tuned to the $D_{3/2} \leftrightarrow P_{1/2}$ repumping transition to decouple the metastable $D_{3/2}$ state from the cooling cycle. The trap consists of two opposite pairs of blade-shaped electrodes and a pair of endcap-shaped electrodes, with characteristic distances of $2r_0 = 1.6$ mm and $2z_0 = 5.5$ mm for the blade and endcap electrodes, respectively [24] (based on Ref. [25]). Radial confinement in the xy plane is accomplished by driving a pair of opposite blades with a radio-frequency (rf) field with $\omega_{\rm rf} = 2\pi \times 21.9$ MHz while keeping the other pair at ground. Axial confinement along the z axis is achieved by applying a DC voltage U to the endcap electrodes (EC1 and EC2 in Fig. 1). The frequency ω_z is proportional to $\sqrt{U}$. The

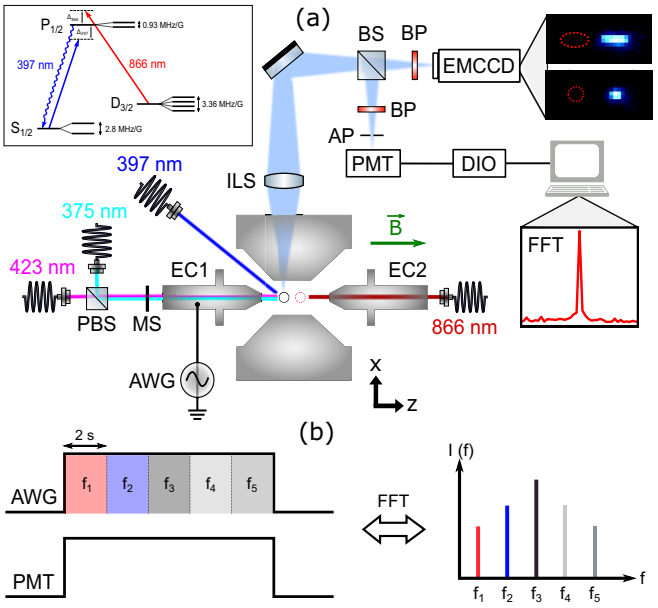

FIG. 1. (a) Sketch of the experimental setup for production, Doppler cooling, and identification of $^{A}Ca^+$ - $^{40}Ca^+$ crystals. The energy levels and transitions employed for Doppler cooling and detection of Ca^+ are shown in the inset. The separation distance between the dark (dashed red circle) and bright ions is $D \approx 8$ μm. (b) Variation of the excitation-field radio frequency around resonance and expected frequency spectrum from the PMT detected signal.

trapping voltages are set such that the oscillation frequencies of a single trapped $^{40}Ca^+$ ion are $\omega_{x,y} \simeq 2\pi \times 1.5$ MHz and $\omega_z \simeq 2\pi \times 0.6$ MHz. A dipolar electric field with amplitude $V_{\rm dip}$ can be applied between EC1 and EC2 by means of an arbitrary function generator (AWG), varying the radio frequency following the comblike pattern of Fig. 1(b). The Ca^+ ions were produced near the trap center through two-step photoionization of Ca atoms vaporized from a resistively heated source filled with natural calcium. A free-running diode laser at 375 nm and a tunable diode laser at 423 nm were used. The latter was tuned to the corresponding resonance of the $^1S_0 \leftrightarrow {}^1P_1$ transition in Ca to selectively produce the ion of interest [26]. All tunable lasers were stabilized in frequency using a 10-MHz-accurate wavemeter [27]. The 397-nm fluorescence photons were collected by an imaging lens system (ILS) and split into two branches by a 50:50 beamsplitter (BS) to detect simultaneously the fluorescence signal with an EMCCD camera and a PMT. The EMCCD camera provides spatially resolved signals that allow certifying the production and characterizing the excitation of calcium crystals [top right of Fig. 1(a)]. The 397-nm photons were recorded with the PMT for a detection time $t_{\rm PMT}$ and time-stamped by a digital input/output (DIO) board. The full experiment is controlled and automated by ARTIQ [28].

III. MEASUREMENTS, RESULTS, AND DISCUSSION

Single ions and two-ion crystals were resonantly excited [an example is shown in the top right of Fig. 1(a)] by applying an external dipolar field introducing a modulation of the

fluorescence intensity $\delta F(v_z) \propto v_{z,0}\cos(\omega_z t)$ such that

$$F = \Gamma\,\rho_{ee}(v_z) \simeq \Gamma[\,\rho_{ee,0} + \delta\rho_{ee}(v_z)] = F_0 + \delta F(v_z), \quad (2)$$

where Γ and $\rho_{ee}(v_z)$ are the spontaneous decay rate and the velocity-dependent occupation probability of the excited state ($P_{1/2}$), respectively. $\rho_{ee,0}$ and F_0 are the (approximately) constant occupation probability and fluorescence rate at the Doppler limit.

The frequencies ω_z and Ω_z^- are measured with the setup through the following experimental sequence. We first produce and cool the single $^{40}Ca^+$ ion to the Doppler limit. Then, we apply the five-radio-frequency field around ω_z with fixed amplitude and acquire the fluorescence signal in parallel. After this measurement, we properly tune the 423-nm laser to produce a single $^{A}Ca^+$ isotope and form the $^{A}Ca^+$ - $^{40}Ca^+$ ion crystal in order to determine Ω_z^-. The formation of the crystal is certified by monitoring the fluorescence signal with the EMCCD camera until the fluorescing ion moves away from the trap center due to the Coulomb interaction between the ions [see the images in Fig. 1(a)]. After the crystal is formed, we apply the excitation field around Ω_z^- and again acquire the corresponding fluorescence signal. The 397- and 866-nm beams were continuously applied to the ions during the entire sequence.

The frequencies ω_z and Ω_z^- are determined through the discrete fast Fourier transform (FFT) of the detected PMT signal after applying the comblike radio-frequency field shown in Fig. 1(b). Considering a data array of length n_b with inputs x_m that are evenly spaced in time by samples of size n_s, the discrete FFT of such input is

$$\mathrm{FFT}_k = \sum_{m=0}^{n_b-1} x_m \exp\left(-2\pi i \frac{mk}{n_b}\right), \quad k = 0, 1, \ldots, n_b - 1. \quad (3)$$

This transform maps the components of the input signal onto a spectrum of discrete frequencies f_l given by

$$f_l = l\,f_r, \quad l = -n_b/2, \ldots, n_b/2, \quad (4)$$

where $f_r = 1/(n_b n_s)$ is the frequency resolution of the Fourier spectrum and $f_s = 1/b_s$ is the sampling frequency. The transform satisfies $\mathrm{FFT}_{n_b-k} = \mathrm{FFT}_k^*$; hence, the value of the FFT for positive frequencies is the conjugate of the values for negative frequencies. This symmetry is exploited to efficiently compute the FFT only for positive values of f_l.

We analyze the signal recorded during a time window $t_w = n_b n_s$ that may be a submultiple of the PMT acquisition time, i.e., $t_w = t_{PMT}/n$. The acquired dataset consists of five intervals, one for each tooth of the radio-frequency comb. The data analysis comprises the following steps:

(1) Compute a histogram of the time-stamped counts with a temporal size of $b_s = 250$ ns and a time window of $t_w = t_{PMT} = 10\,s$, yielding a dataset with a resolution of $f_r = 0.1$ Hz and sampling frequency of $f_s = 4$ MHz. This choice allows us to sample signals of up to 2 MHz for different values of t_w [29].

(2) Split the histogram into $n_s = 5$ intervals, each of them containing information on a single frequency f_i of the radio-frequency comb and corresponding to a time window of $t_{rf} = 2$ s.

(3) If $t_w < 10$ s, split the histograms into n subintervals, each of them corresponding to a time window of t_{rf}/n.

(4) Perform the zero padding of the individual intervals to maintain the frequency resolution of $f_r = 0.1$ Hz.

(5) Compute the magnitude of the FFT, i.e., $|\mathrm{FFT}|_n$ for each of the n subhistograms.

(6) For each of the n_s slices, select a single FFT spectrum with magnitude $|\mathrm{FFT}|_{n_s}$ among the n subhistograms and then sum the n_s FFT spectrums. This operation yields an individual measurement with a time window of $t_w = t_{PMT}/n$ and an excitation window of $t_{rf} = t_w/n_s = t_{PMT}/(n_s\,n)$.

(7) Compute the frequencies f_l of the FFT spectrum with $f_r = 0.1$ Hz and find the FFT intensities at the position of the radio frequencies f_i.

(8) Perform a Lorentzian fit by considering the five peaks as the input data and setting the offset of the fitting function to the mean background of the signal. The width, center, and area of the Lorentzian are set as free parameters.

FFT signals for different unbalanced two-ion crystals are shown in Figs. 2(a) and 2(c) for an endcap-driving amplitude $V_{dip} = 2$ mV_{pp}. At the trap center, this results in an effective driving amplitude of 1.4 μV with a peak electric field of 3.4 μV/μm. The fluorescence signal was recorded with the PMT for $t_{PMT} = 10$ s (equal to t_w in this case). The frequency-resolving power $\Omega_z/\Delta\Omega_{z,FWHM} = 620$ results in a mass-resolving power $m/\Delta m_{FWHM} \approx 310$. Figure 2(b) shows the axial oscillation of the sensor ion, obtained from the EMCCD image, for the different data points (comb frequencies) of Fig. 2(a). The maximum oscillation amplitude z_s^{max} goes from 1.14(2) to 4.95(3) μm for the minimum and maximum FFT intensities, respectively. These amplitudes correspond to kinetic energies of about 40 and 720 mK, respectively. Figure 3 shows FFT signals from shorter individual measurements with $t_w = 500$ ms (consisting of five subintervals of 100 ms) and 100 ms (five subintervals of 20 ms) and $V_{dip} = 3$ mV_{pp}. Featured peaks are always observed even for $t_w = 100$ ms, although fitting curves were obtained only when $t_w \geqslant 500$ ms for 3 mV_{pp}, as shown in Fig. 3.

The signal-to-noise ratio (SNR) of a particular peak in the FFT spectra is computed as

$$\mathrm{SNR} = \frac{S - B}{\Delta B_{FWHM}}, \quad (5)$$

where S represents the height of the peak, B is the mean intensity of the background signal, and ΔB_{FWHM} corresponds to the FWHM fluctuations of the background signal. Figure 4 shows the evolution of the SNR of the most intense peak at f_3 with the time window t_w for the $^{A}Ca^+$-$^{40}Ca^+$ crystals. Each data point corresponds to an average of 10 measurements, and the error bars represent 1σ deviations from the mean values. The left (right) panel of Fig. 4 corresponds to an excitation amplitude of 2 (3) mV_{pp}, whereas the shaded areas outline the time windows where the Lorentzian fit to the data was not possible.

Alternating frequency measurements with single Doppler-cooled ions and two-ion crystals were performed to evaluate the optical mass identification method with the setup in Fig. 1. A reference measurement of ω_z with a single Doppler-cooled $^{40}Ca^+$ ion was carried out before (at time t_{i-1}) and after (t_{i+1}) a measurement of Ω_z^- of a $^{A}Ca^+$-$^{40}Ca^+$ crystal at time t_i to

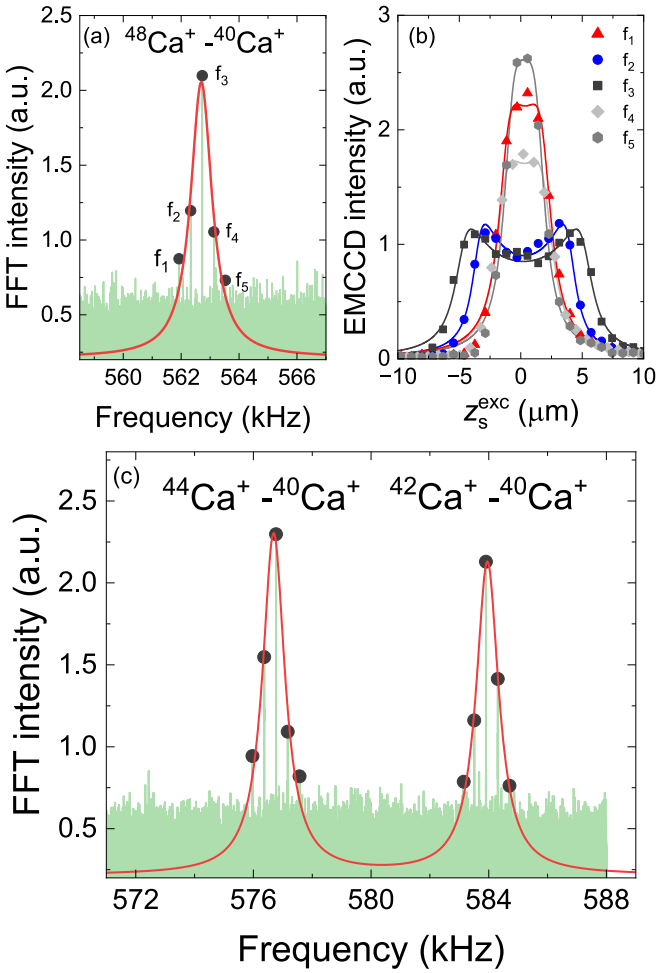

FIG. 2. (a) FFT of the detected photons from f_1 to f_5 in Fig. 1(b) around Ω_z^- (f_3) for $^{48}Ca^+$ - $^{40}Ca^+$. The solid circles indicate the FFT intensities for excitations at f_1 to f_5. The red solid curve is a Lorentzian fit considering these data points and the average background level. (b) Axial projections of the EMCCD images when applying the radio-frequency-comb spectrum shown in Fig. 1(b). The solid lines are fits following the function derived in Ref. [30]. (c) The same as (a) for independent measurements with $^{44}Ca^+$ - $^{40}Ca^+$ and $^{42}Ca^+$ - $^{40}Ca^+$. Each spectrum is extracted from a single measurement with $t_w = 10$ s.

account for fluctuations of the voltage U or any other possible factors that perturb ω_z and Ω_z^-. Each measurement in turn consisted of 10 consecutive measurements with $t_{PMT} = 10$ s each. A linear interpolation between the two reference measurements of ω_z was performed at times t_{i-1} and t_{i+1} to obtain ω_z at t_i and, in this way, the ratio $\xi(t_i) = \Omega_z^-(t_i)/\omega_z(t_i)$. Recalling Eq. (1) and considering $q_s = q_t = 1$, the frequency ratio (in the linear approximation) can be calculated from known mass values as [13]

$$\xi = \sqrt{1 + \frac{1}{\mu} - \sqrt{1 + \frac{1}{\mu^2} - \frac{1}{\mu}}}, \tag{6}$$

with

$$\delta\xi(t_i) = \xi(t_i)\sqrt{[\delta\Omega_z^-(t_i)/\Omega_z^-(t_i)]^2 + [\delta\omega_z(t_i)/\omega_z(t_i)]^2}. \tag{7}$$

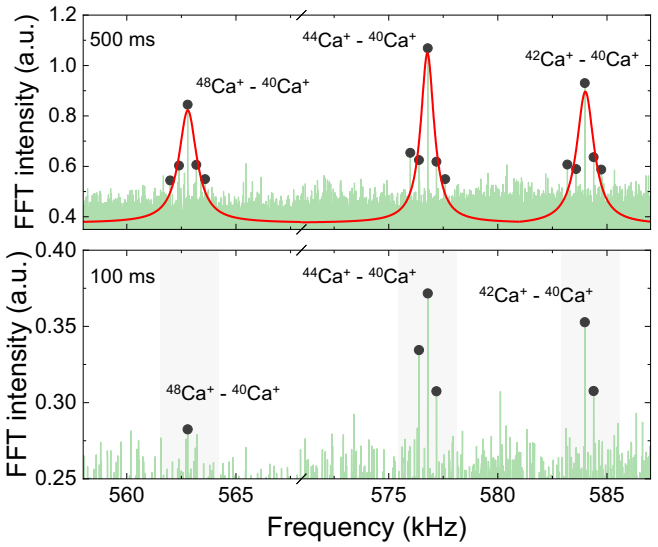

FIG. 3. FFT of the detected photons for $^A Ca^+$ - $^{40}Ca^+$ ($A = 42, 44, 48$) from single measurements with $t_w = 500$ ms (top) and $t_w = 100$ ms (bottom). The amplitude of the dipolar field is 3 mV_{pp}. The red solid curve is a Lorentzian fit to the data. A partial response to the radio-frequency comb is still observed when $t_w = 100$ ms.

The relative deviations of the measured ratios ξ_{exp} [$\xi(t_i)$] with respect to the expected values ξ_{bib} for the $^A Ca^+$-$^{40}Ca^+$ crystals with $m_s/q_s = 40$ were evaluated and are shown in the left panel of Fig. 5. The ratios ξ_{bib} are obtained after substituting the values of μ from the literature data [31,32] in Eq. (6). The measurements were carried out for several amplitudes of the excitation field ($V_{dip} = 2$, 3, 4, and 5 mV_{pp}). The results for the $^{42}Ca^+$-$^{40}Ca^+$ crystal agree with the expected values within an uncertainty on the order of 10^{-4} in all cases. Under approximately the same experimental conditions, $(\xi_{exp} - \xi_{bib})/\xi_{bib}$ deviates more than 1σ (but less than 2σ) for the $^{44}Ca^+$ - $^{40}Ca^+$ and $^{48}Ca^+$ - $^{40}Ca^+$ crystals for the smallest excitation amplitude. This shift becomes larger than

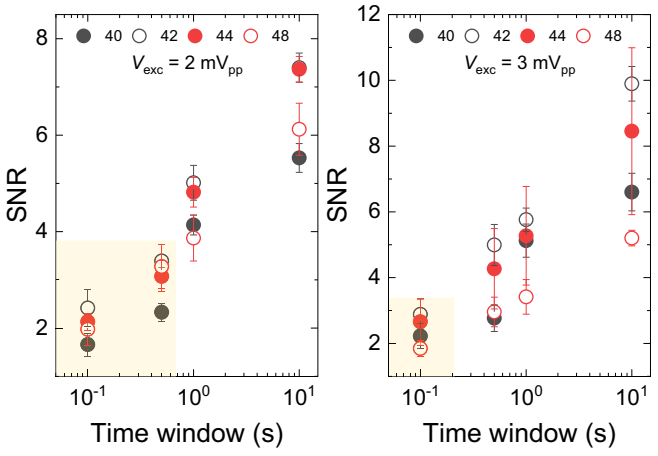

FIG. 4. Signal-to-noise ratio of the most intense peak in the FFT as a function of the time window t_w for excitation amplitudes of 2 mV_{pp} (left) and 3 mV_{pp} (right). The shaded areas depict the timescales when the Lorentzian fit could not be performed.

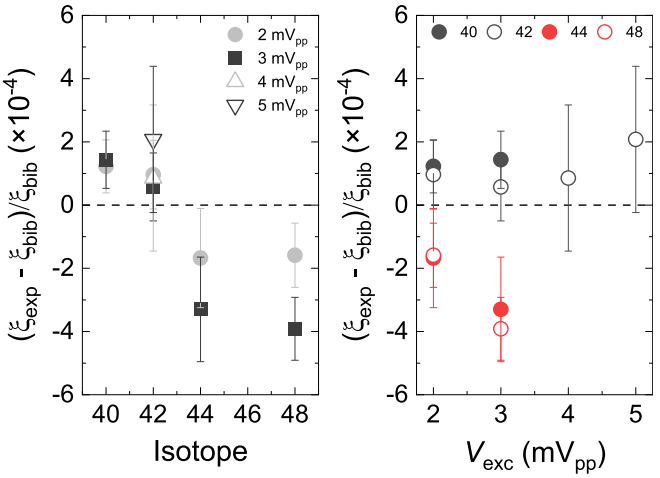

FIG. 5. Left: Relative deviation of ξ_{exp} with respect to ξ_{bib} for ^{A}Ca^{+} - ^{40}Ca^{+} crystals and different excitation amplitudes. Right: The same, but as a function of V_{dip}. $t_w = 10$ s for these measurements. The same behavior was observed when $t_w = 1$ s. When $V_{dip} \geqslant 4$ mV$_{pp}$, the ordered structures of the ^{44}Ca^{+} - ^{40}Ca^{+} and ^{48}Ca^{+} - ^{40}Ca^{+} crystals vanish for the central frequency of the comb, and the Lorentzian fits fail; therefore, no results for these cases are shown. For further details see the Appendix.

2σ for $V_{dip} = 3$ mV$_{pp}$, as shown in the right panel of Fig. 5. It might be considered mass dependent, although the uncertainties overlap. If $V_{dip} \geqslant 4$ mV$_{pp}$, the ordered structure remains only for the ^{42}Ca^{+}-^{40}Ca^{+} crystal (see the Appendix). z_s^{max}, defined as the oscillation amplitude for z_s^{exc} shown, e.g., in Fig. 2 for a ^{48}Ca^{+}-^{40}Ca^{+} crystal driven with $V_{dip} = 2$ mV$_{pp}$, increases as a function of V_{dip}. For the ^{42}Ca^{+}-^{40}Ca^{+} crystal, the largest z_s^{max} ranged from 5.70(3) to 17.4(1) μm for the V_{dip} values in Fig. 5. These amplitudes are, in most cases, larger than the distance between the two ions in the unperturbed crystal, about 8 μm.

The effect of the Coulomb interaction on increasing the oscillation amplitude of the ions in the crystal has been considered as a source for this systematic shift. Numerical calculations were carried out considering only the axial modes and no influence of the radio-frequency trapping field. The systematic frequency shifts observed due to the excitation of the crystals are proportional to z_s^2, with a proportionality constant depending on the mass difference $C(m_t - m_s)$, assuming $q_s = q_t = 1$. However, they are below those observed in the experiments and have opposite sign, which suggests a different reason than the Coulomb interaction or anharmonicities in symmetric potentials [33]. The effect of the constant radiation-pressure force induced by the red-detuned laser was also considered. It would lead to a displacement of the ions from their expected equilibrium positions by an amount δz_{laser} that can shift the eigenfrequencies of the two-ion system proportionally in first order to $\delta z_{laser}/D$ [34]. Frequency shifts on the order of 1×10^{-5} or smaller have been obtained for the range of masses studied in this paper, which is negligible compared to the statistical uncertainty of the measurements. This suggests that the deviations observed for the ^{44}Ca^{+} - ^{40}Ca^{+} and ^{48}Ca^{+} - ^{40}Ca^{+} crystals, which increase with the oscillation amplitudes, are associated with other effects.

IV. SUMMARY AND OUTLOOK

In this paper we demonstrated the nondestructive identification of sympathetically cooled ions in a linear trap using a radio-frequency comblike structure that excites the axial motion of the two-ion crystal. The method is fast and sufficient to discriminate between atomic species of the periodic table with a mass-resolving power $m/\Delta m_{FWHM} \approx 310$, providing at the same time a platform for single-ion laser spectroscopy. Single measurements within times below 1 s can provide the mass identification in a regime with minimum disturbances due to the Coulomb interaction.

We implemented a sequence to measure the axial frequency of an individual laser-cooled ion (sensor ion) before and after the axial-common-mode frequency of the unbalanced crystal, formed by the sensor and a "dark" target ion, to evaluate the mass identification method. When $m_t - m_s < 4$, the motional frequency ratios follow Eq. (6) with a relative uncertainty of 10^{-4}. When $m_t - m_s \geqslant 4$, it deviates when increasing the oscillation amplitude of the ions. The outcomes from simulations showed that the effect of the Coulomb interaction on the axial modes is not visible in the measurements presented in this paper and the deviations observed when increasing the oscillation amplitudes of the ion in the crystal have to be attributed to other factors, which might be mass dependent. This is important when using this method for larger differences between the mass-to-charge ratios of the target and sensor ions. Heavier ions will need other ion species which have Doppler-cooling schemes similar to Ca^{+}, like ^{86,87,88}Sr^{+} or $^{134-138}$Ba^{+}, to measure SHEs (with $A \approx 258$) with charge states of 3^{+} and 2^{+}, respectively, in order to keep $m_t/q_t - m_s/q_s$ smaller and thus prevent large systematic shifts.

If the conditions in the trap are highly stable, one single-ion identification can be performed prior to a laser-spectroscopy experiment or after, e.g., resonance ionization spectroscopy, improving the sensitivity of the latter by orders of magnitude. Although our method is conceptually feasible for application to SHEs, the linear Paul trap should be placed in a beamline where the target ion can be introduced with high efficiency. This requires a cryogenic buffer-gas stopping cell [35] to thermalize the ions and extract and guide them at very low energies into a preparation trap such as a radio-frequency-quadrupole (RFQ) buncher to produce pulses for efficient injection in the linear Paul trap. The Penning trap facility SHIPTRAP has these elements [36], and the coupling of such a system can be done after the RFQ buncher by means of electrostatic optics. In terms of measurement time, the limitation will arise mainly from the time to sympathetically cool the target ion, which will depend strongly on the energy of the ion with respect to the trap bottom. Investigations of this aspect are important because that time will limit the accessible isotopes according to their half-life. Considering sympathetic-cooling times on the order of a few seconds, measurements in the superheavy-element region are still possible.

It is worth mentioning that the results from the axial motion can be projected to a Penning trap [37], preventing possible perturbative effects due to the radio-frequency field and extending the frequency measurements beyond the axial-common mode. Very recently, the frequencies of all

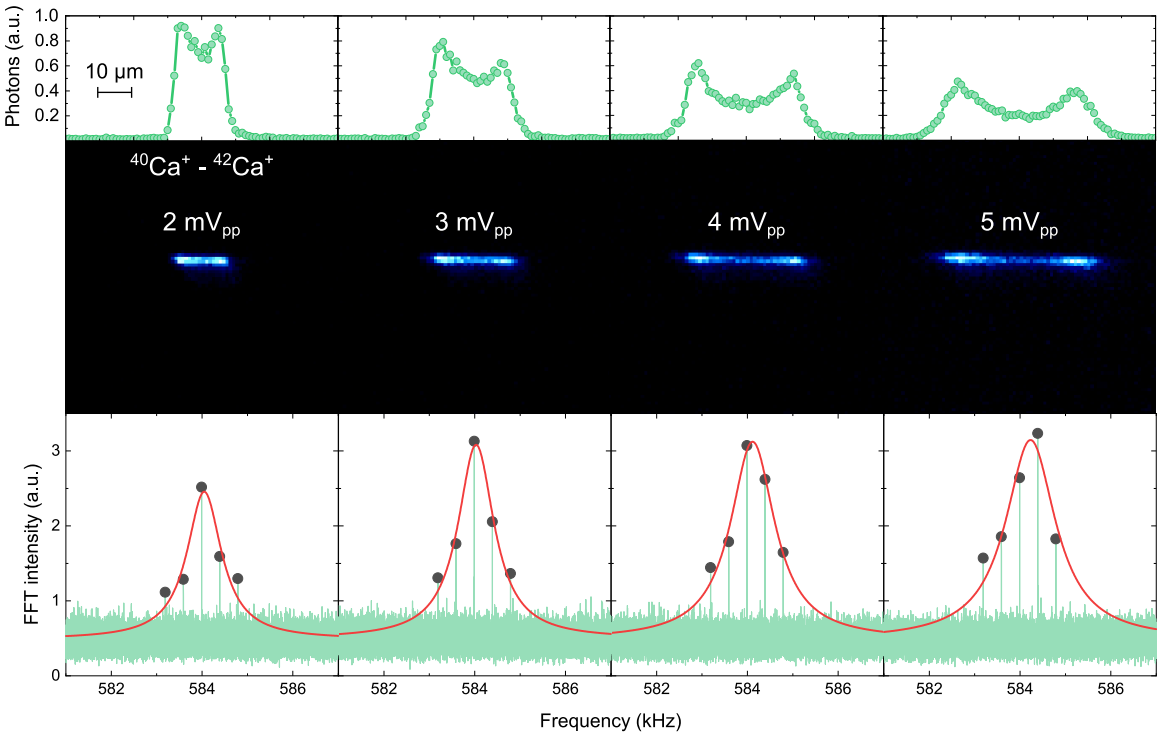

FIG. 6. EMCCD images and axial distributions of the $^{42}Ca^+$ - $^{40}Ca^+$ crystals at the maximum amplitude z_s^{max} (f_3). The images are ordered for increasing values of V_{dip} from left to right. The bottom panels show the FFT signals from the full comb (f_1–f_5) and the Lorentzian fits.

motional modes (common and stretch) of the $^{42}Ca^+$ - $^{40}Ca^+$ crystal were measured in a 7-T Penning trap [38] using the fluorescence photons through the detected EMCCD images or PMT counts as done for a single ion in Ref. [32]. These measurements needed a large excitation amplitude, showing strong nonlinearities in many of the resonance profiles and thus a large deviation of the cyclotron frequency of the target ion obtained from the generalized invariance theorem [39], compared to the value obtained from a single-ion measurement in the same experiment. The technique presented in this paper will need only small oscillation amplitudes (kinetic energies) to perform a cyclotron-frequency measurement.

ACKNOWLEDGMENTS

We acknowledge support from Grant No. PID2022-141496NB-I00 funded by MICIU/AEI/10.13039/501100011033 and by ERDF/EU, Grant No. PID2019-104093GB-I00 funded by MICIU/AEI/10.13039/501100011033; from FEDER/Junta de Andalucía - Consejería de Universidad, Investigación e Innovación through Project No. P18-FR-3432; from Programa "Yo Investigo" Junta de Andalucía-Next Generation EU; and from the University of Granada "Laboratorios Singulares 2020." The construction of the Ion Traps and Lasers Laboratory was supported by the European Research Council (Contract No. 278648-TRAPSENSOR); Projects No. FPA2015-67694-P (funded by MICIU/AEI/10.13039/501100011033, and by ERDF A way of making Europe) and No. FPA2012-32076 (MICIU/FEDER): Infrastructure Projects No. UNGR10-1E-501, No. UNGR13-1E-1830 (MICIU/FEDER/UGR), and No. EQC2018-005130-P (funded by MICIU/AEI/10.13039/501100011033, and by ERDF A way of making Europe); and Infrastructure Projects No. INF-2011-57131, No. IE2017-5513 and No. IE19_204 UGR (funded by Junta de Andalucía/FEDER).

APPENDIX: NOTES ON THE ANALYSIS FOR HIGH OSCILLATION AMPLITUDES

This Appendix shows the criteria used to discard experimental data in the evaluation of the results after the analysis. Data were discarded when the crystal structure was broken. That is the case for the central frequency of the comb (f_3) for the $^{44}Ca^+$ - $^{40}Ca^+$ and $^{48}Ca^+$ - $^{40}Ca^+$ crystals at $V_{dip} = 4$ and 5 V_{pp} but not for $^{42}Ca^+$ - $^{40}Ca^+$ (see Figs. 6 and 7). As shown in Fig. 7 for the $^{48}Ca^+$ - $^{40}Ca^+$ crystal, the FFT signal at the comb frequency closest to resonance f_3 (crystal broken) is smaller than the FFT signal at other frequencies further away from resonance, for which the crystal structure remains. In this case, the Lorentzian fit is shifted by a few hundred hertz, yielding results which deviate from the correct values. That is the case for all measurements on $^{44}Ca^+$ - $^{40}Ca^+$ and $^{48}Ca^+$ - $^{40}Ca^+$ at $V_{dip} = 4$ and 5 V_{pp}. Data were also discarded when a clear asymmetry was observed in the FFT spectrum, indicating that the frequency of the dipolar field applied deviated more than 800 Hz (twice the frequency step of the comb). In such cases one cannot state which is the maximum FFT signal, and only part of the Lorentzian profile can be obtained. This, however, can be overcome in future experiments by increasing the frequency width of the comb up to a factor of 10 (20 kHz), maintaining the frequency step

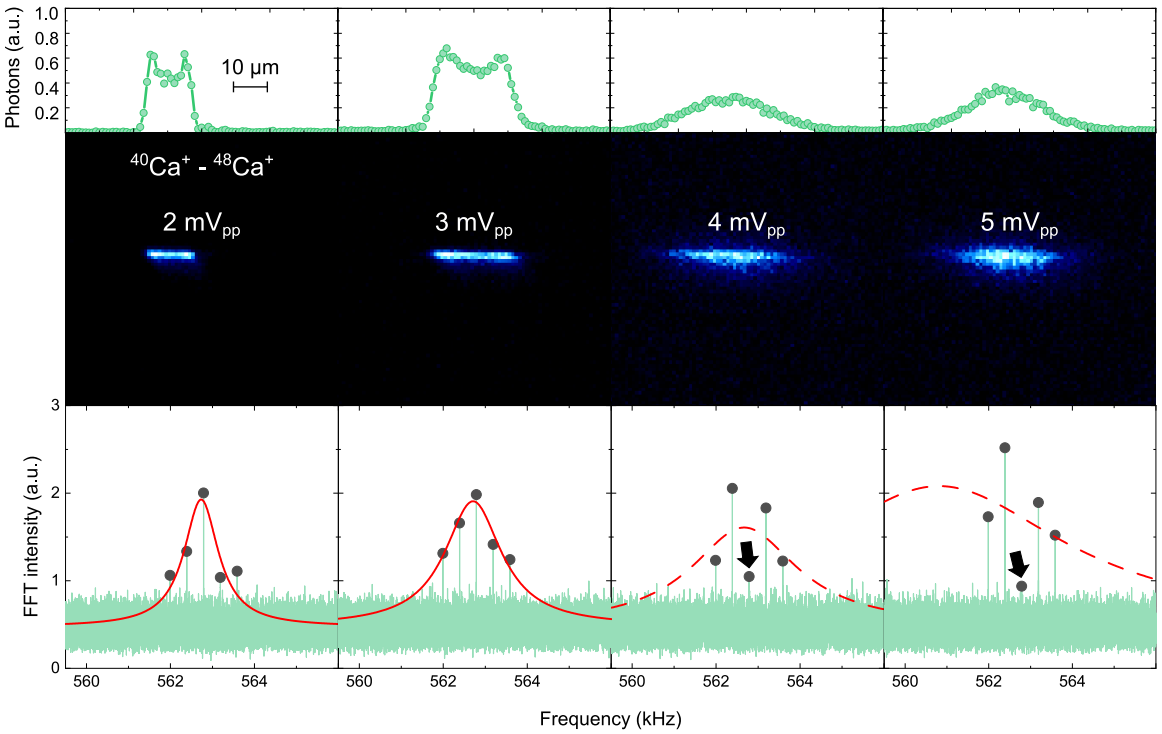

FIG. 7. EMCCD images and axial distributions of the $^{48}Ca^{+}$ - $^{40}Ca^{+}$ crystals at the maximum amplitude z_s^{max}. The images are ordered for increasing values of V_{dip} from left to right. The crystal is melted for the largest amplitude (frequency f_3) at $V_{dip} = 4$ and 5 V_{pp}, decreasing the intensity (for f_3) indicated by the thick black arrow, preventing the Lorentzian fit.

of 400 Hz and $t_{PMT} = 10$ s (200 ms per frequency step), which still provides a sufficient signal-to-noise ratio to perform the five-point Lorentzian fit with the minimum endcap-driving amplitude.

[1] O. R. Smits, P. Indelicato, W. Nazarewicz, M. Piibeleht, and P. Schwerdtfeger, Pushing the limits of the periodic table – A review on atomic relativistic electronic structure theory and calculations for the superheavy elements, Phys. Rep. **1035**, 1 (2023).

[2] O. R. Smits, C. E. Düllmann, P. Indelicato, W. Nazarewicz, and P. Schwerdtfeger, The quest for superheavy elements and the limit of the periodic table, Nat. Rev. Phys. **6**, 86 (2024).

[3] M. Block, M. Laatiaoui, and S. Raeder, Recent progress in laser spectroscopy of the actinides, Prog. Part. Nucl. Phys. **116**, 103834 (2021).

[4] M. Drewsen, Cooling, identification and spectroscopy of superheavy element ions, Eur. Phys. J. D **45**, 125 (2007).

[5] M. Drewsen, A. Mortensen, R. Martinussen, P. Staanum, and J. L. Sørensen, Nondestructive identification of cold and extremely localized single molecular ions, Phys. Rev. Lett. **93**, 243201 (2004).

[6] T. B. Takashi Baba and I. W. Izumi Waki, Cooling and mass-analysis of molecules using laser-cooled atoms, Jpn. J. Appl. Phys. **35**, L1134 (1996).

[7] C. Schneider, S. J. Schowalter, K. Chen, S. T. Sullivan, and E. R. Hudson, Laser-cooling-assisted mass spectrometry, Phys. Rev. Appl. **2**, 034013 (2014).

[8] S. Sels, F. M. Maier, M. Au, P. Fischer, C. Kanitz, V. Lagaki, S. Lechner, E. Leistenschneider, D. Leimbach, E. M. Lykiardopoulou, A. A. Kwiatkowski, T. Manovitz, Y. N. Vila Gracia, G. Neyens, P. Plattner, S. Rothe, L. Schweikhard, M. Vilen, R. N. Wolf, and S. Malbrunot-Ettenaue, Doppler and sympathetic cooling for the investigation of short-lived radioactive ions, Phys. Rev. Res. **4**, 033229 (2022).

[9] S. Schlemmer, J. Illemann, S. Wellert, and D. Gerlich, Nondestructive high-resolution and absolute mass determination of single charged particles in a three-dimensional quadrupole trap, J. Appl. Phys. **90**, 5410 (2001).

[10] P. Bowe, L. Hornekær, C. Brodersen, M. Drewsen, J. S. Hangst, and J. P. Schiffer, Sympathetic crystallization of trapped ions, Phys. Rev. Lett. **82**, 2071 (1999).

[11] K. Mølhave and M. Drewsen, Formation of translationally cold MgH^{+} and MgD^{+} molecules in an ion trap, Phys. Rev. A **62**, 011401(R) (2000).

[12] M. Gutiérrez, Studying an unbalanced two-ion crystal in a Penning trap: Towards the quantum regime in a high magnetic field, Ph.D. thesis, Universidad de Granada, 2021.

[13] G. Morigi and H. Walther, Two-species Coulomb chains for quantum information, Eur. Phys. J. D **13**, 261 (2001).

[14] D. J. Larson, J. C. Bergquist, J. J. Bollinger, W. M. Itano, and D. J. Wineland, Sympathetic cooling of trapped ions: A laser-cooled two-species nonneutral ion plasma, Phys. Rev. Lett. **57**, 70 (1986).

[15] P. F. Staanum, K. Højbjerre, R. Wester, and M. Drewsen, Probing isotope effects in chemical reactions using single ions, Phys. Rev. Lett. **100**, 243003 (2008).

[16] K. Sheridan and M. Keller, Weighing of trapped ion crystals and its applications, New J. Phys. **13**, 123002 (2011).

[17] J. E. Goeders, C. R. Clark, G. Vittorini, K. Wright, C. R. Viteri, and K. R. Brown, Identifying single molecular ions by resolved sideband measurements, J. Phys. Chem. A **117**, 9725 (2013).

[18] K. Groot-Berning, F. Stopp, G. Jacob, D. Budker, R. Haas, D. Renisch, J. Runke, P. Thörle-Pospiech, C. E. Düllmann, and F. Schmidt-Kaler, Trapping and sympathetic cooling of single thorium ions for spectroscopy, Phys. Rev. A **99**, 023420 (2019).

[19] M. Fan, C. A. Holliman, X. Shi, H. Zhang, M. W. Straus, X. Li, S. W. Buechele, and A. M. Jayich, Optical mass spectrometry of cold $RaOH^+$ and $RaOCH_3^+$, Phys. Rev. Lett. **126**, 023002 (2021).

[20] K. Saito, R. Saito, and T. Mukaiyama, Ion trap frequency measurement from fluorescence dynamics, J. Appl. Phys. **132**, 094401 (2022).

[21] M. Block, D. Ackermann, K. Blaum, C. Droese, M. Dworschak, S. Eliseev, T. Fleckenstein, E. Haettner, F. Herfurth, F. P. Heßberger, S. Hofmann, J. Ketelaer, J. Ketter, H.-J. Kluge, G. Marx, M. Mazzocco, Yu. N. Novikov, W. R. Pla, A. Popeko, S. Rahaman *et al.*, Direct mass measurements above uranium bridge the gap to the island of stability, Nature (London) **463**, 785 (2010).

[22] E. M. Ramirez, D. Ackermann, K. Blaum, M. Block, C. Droese, C. E. Düllmann, M. Dworschak, M. Eibach, S. Eliseev, E. Haettner, F. Herfurth, F. Heßberger, S. Hofmann, J. Ketelaer, G. Marx, M. Mazzocco, D. Nesterenko, Y. Novikov, W. Plaß, D. Rodríguez *et al.*, Direct mapping of nuclear shell effects in the heaviest elements, Science **337**, 1207 (2012).

[23] O. Kaleja, B. Anđelić, O. Bezrodnova, K. Blaum, M. Block, S. Chenmarev, P. Chhetri, C. Droese, C. E. Düllmann, M. Eibach, S. Eliseev, J. Even, P. Filianin, F. Giacoppo, S. Götz, Y. Gusev, M. J. Gutiérrez, F. P. Heßberger, N. Kalantar-Nayestanaki, J. J. W. van de Laar *et al.*, Direct high-precision mass spectrometry of superheavy elements with SHIPTRAP, Phys. Rev. C **106**, 054325 (2022).

[24] J. Berrocal, Implementación de una trampa lineal para simulaciones del modelo cuántico de Rabi, Master's thesis, Universidad de Granada, 2018.

[25] C. Hempel, Digital quantum simulation, Schrödinger cat state spectroscopy and setting up a linear ion trap, Ph.D. thesis, University of Innsbruck, 2014.

[26] D. M. Lucas, A. Ramos, J. P. Home, M. J. McDonnell, S. Nakayama, J.-P. Stacey, S. C. Webster, D. N. Stacey, and A. M. Steane, Isotope-selective photoionization for calcium ion trapping, Phys. Rev. A **69**, 012711 (2004).

[27] F. Domínguez, J. Bañuelos, J. Berrocal, J. J. del Pozo, M. Hernández, A. Carrasco-Sanz, J. Cerrillo, P. Escobedo-Araque, and D. Rodríguez, A frequency comb stabilized Ti:Sa laser as a self-reference for ion-trap experiments with a $^{40}Ca^+$ ion, Rev. Sci. Instrum. **93**, 093304 (2022).

[28] S. Bourdeauducq, whitequark, R. Jördens, D. Nadlinger, Y. Sionneau, and F. Kermarrec, ARTIQ: A leading-edge control system for quantum information experiments (2021), https://zenodo.org/records/6619071.

[29] C. E. Shannon, Communication in the presence of noise, Proc. IRE **37**, 10 (1949).

[30] F. Domínguez, M. J. Gutiérrez, I. Arrazola, J. Berrocal, J. M. Cornejo, J. J. Del Pozo, R. A. Rica, S. Schmidt, E. Solano, and D. Rodríguez, Motional studies of one and two laser-cooled trapped ions for electric-field sensing applications, J. Mod. Opt. **65**, 613 (2018).

[31] M. Wang, W. J. Huang, F. G. Kondev, G. Audi, and S. Naimi, The AME 2020 atomic mass evaluation (II). Tables, graphs and references, Chin. Phys. C **45**, 030003 (2021).

[32] J. Berrocal, A. Hernández, I. Arrazola, F. Domínguez, A. Carrasco-Sanz, F. J. Fernández, M. Block, and D. Rodríguez, Penning-trap eigenfrequency measurements with optical radiofrequency detectors, Phys. Rev. Res. **6**, L012001 (2024).

[33] J. P. Home, D. Hanneke, J. D. Jost, D. Leibfried, and D. J. Wineland, Normal modes of trapped ions in the presence of anharmonic trap potentials, New J. Phys. **13**, 073026 (2011).

[34] P. Staanum, Quantum optics with trapped calcium ions, Ph.D. thesis, University of Aarhus, 2004.

[35] O. Kaleja, B. Anđelić, K. Blaum, M. Block, P. Chhetri, C. Droese, Ch. E. Düllmann, M. Eibach, S. Eliseev, J. Even, S. Götz, F. Giacoppo, N. Kalantar-Nayestanaki, M. Laatiaoui, E. Minaya Ramirez, A. Mistry, T. Murböck, S. Raeder, L. Schweikhard, and P. G. Thirolf, The performance of the cryogenic buffer-gas stopping cell of SHIPTRAP, Nucl. Instrum. Methods Phys. Res. Sect. B **463**, 280 (2020).

[36] M. Block, D. Ackermann, D. Beck, K. Blaum, M. Breitenfeldt, A. Chauduri, A. Doemer, S. Eliseev, D. Habs, S. Heinz, F. Herfurth, F. P. Heßberger, S. Hofmann, H. Geissel, H. -J. Kluge, V. Kolhinen, G. Marx, J. B. Neumayr, M. Mukherjee, M. Petrick *et al.*, The ion-trap facility SHIPTRAP, Eur. Phys. J. A **25**, 49 (2005).

[37] M. J. Gutiérrez, J. Berrocal, F. Domínguez, I. Arrazola, M. Block, E. Solano, and D. Rodríguez, Dynamics of an unbalanced two-ion crystal in a Penning trap for application in optical mass spectrometry, Phys. Rev. A **100**, 063415 (2019).

[38] J. Berrocal, A. Hernández, D. Porras, and D. Rodríguez, Laser-assisted motional-mode spectroscopy in a Penning trap and the generalized invariance theorem, Phys. Rev. A **110**, 063107 (2024).

[39] S. Jain, J. Alonso, M. Grau, and J. P. Home, Scalable arrays of micro-Penning traps for quantum computing and simulation, Phys. Rev. X **10**, 031027 (2020).